A one-dimensional reactive transport model of geochemical desalination scaling

Andrew P. Freiburger[1,2] [a], Sergi Molins[2], and Heather L. Buckley[1,3]

[1]*Department of Civil Engineering and* [3]*Centre for Advanced Materials and Related Technology (CAMTEC), University of Victoria, 3800 Finnerty Road, Victoria, BC V8P 5C2, CAN*

[2]*Energy Geosciences Division, Lawrence Berkeley National Laboratory, 1 Cyclotron road, Berkeley, CA*

E-mail:

[a]To whom correspondence should be addressed. Tel: 616-322-8036 ; email: andrewfreiburger@gmail.com

Abstract

Freshwater insecurity afflicts billions of people each year, yet desalination technologies such as Reverse osmosis (RO) can sustainably purify ocean water into a limitless source of potable water. The economical efficiency of RO, however, hinders its practicality. Mineral nucleation on the membrane surface in a process called scaling is specifically problematic for RO modules, but the geochemical mechanisms of scaling (particularly from brackish feed waters) remain elusive to experimental protocols and most simulations of RO systems. We therefore developed a geochemical reactive transport model of RO desalination that simulates one dimension of the feed-membrane interface while resolving the mineral geochemistry that manifests in scaling via robust PHREEQC calculations. This approach balances computational expense and with sufficiently precise results for actionable interpretation. Our model is implemented as an operable Python Software (ROSSpy) that provides users spatiotemporal predictions of scale deposits and concentration changes through the model as a function of specified feed concentrations and conditions, and the RO module specifications. The raw output is additionally visualized to facilitate user interpretation. We exemplify this model through numerous case studies and parameter scans. This concise yet rigorous model provides a unique tool to identify appealing feed waters and to improve RO designs towards developing sustainable water systems in diverse conditions around the world.

Keywords Reverse Osmosis, desalination, geochemistry, reactive transport, scaling

1. Introduction

Potable fresh water is a scarce resource for billions of people,[1–3] ironically despite that water is among the most abundant chemicals on Earth.[4] This scarcity is attributable to arid climates, global warming[5] and climate change[6] that change water patterns, and over-consumption[7] and pollution[8] of civil water sources. The 6th UN Sustainable Development Goal[9] acknowledges the existential importance of potable freshwater as a basic human right, yet technological advances in water infrastructure and filtration are required to realize this vision.

Desalination is a promising tool to generate potable fresh water on demand from diverse and potentially contaminated water supplies, such as the inexhaustible oceans[10] that are conveniently within $100km$ for $\approx \frac{1}{2}$ of the human population.[11] The most common desalination technology is the spiral-wound reverse osmosis (RO) module,[12] whose compact and modular design optimizes its efficient.[13,14] RO utilizes a very fine filtration membrane that diffuses water while blocking impurities: microorganisms, molecules, and even elemental ions. RO is already a municipal staple in arid Middle-Eastern countries; Israel, for example, supplies $\frac{3}{4}$ of its domestic water from desalination[15] and Saudi Arabia is responsible for $\approx 22\%$ of global water desalination.[16] The concentrated effluent from RO fosters poses an environmental hazard? (although this can be mitigated with zero-liquid processing[17–19]) and more critically fosters microbial growth[20–22] and mineral precipitate – scaling[23–26] – at the end of the RO module (processes categorized as membrane fouling[27]) that impede RO efficiency.[11,28,29]

Mineral scaling is particularly challenging[30] as it is ubiquitous, difficult to remove,[31] and expensive[32] and unpredictable to prevent in brackish feed water with antiscalant chemical additives.[33,34] Scaling is further experimentally elusive in situ,[35] notwithstanding recently methods,[36] which hinders basic understanding and therefore technological advancement. Software may supplement experimental limitations,[37] but most RO software either incompletely capture[38,39] or completely ignore[40,41] scaling, and geochemical reactive transport

software[42,43] have not yet been adapted for RO desalination. A few mathematical programs,[44,45] programming interfaces,[46,47] and studies of scaling[48,49] and RO[50–53] simulate the scaling development in an RO module, but these tools do not permit the broad analyses, over a range of feed and module parameters, that are necessary to explore edge cases and to empower researchers with diverse RO setups.

We therefore developed a unique one-dimensional model of RO desalination that captures scaling geochemistry during desalination, unlike existing one-dimensional RO models,[54] and represents the membrane interface via the solution-diffusion model.[47,55] We exemplify the model with spatiotemporal scaling predictions that recapitulate observed scaling from RO plants in Australia,[56] UAE,[57] Tunisia,[58] and Greece.[59,60] We further demonstrate the flexibility of our model by 1) reproducing scaling in a membrane bioreactor,[61] which is similar to RO, and 2) exploring diverse feed water conditions and supported geochemical activity models. We developed an open-source software that implements our model (ROSSpy: RO Scaling Software in Python) by leveraging PHREEQC[62] for geochemical calculations. ROSSpy, to our knowledge, uniquely fulfills solicited needs from the community for simulating RO scaling.[59] We believe that this one-dimensional model and ROSSpy offer important tools for improving RO performance by surmounting scaling, and thereby alleviating water insecurities around the world.

2. Methods

Our model represents RO as a geochemical reactive transport process along one dimension of the membrane-feed interface. A glossary of parameters and variables for the equations and calculations are provided in Table 1. The geochemistry and reactive transport mathematics of our RO model are derived in the following sub-sections.

Table 1: Glossary of ROSSpy variables.

variable	name	description
l	length	longitudinal dimension of the module or module cell
n	number of module cells	quantity of discretizations of the module
Φ_e	moles	the $moles_{H_2O}$ that exist in cell e
$\Delta\Phi_e$	permeate flux	the $moles_{H_2O}$ that are removed in cell e
HL	head loss	reduction of pressure over the module distance
PE	permeate efficiecy	attenuation of permeate flux from pre-existing inefficiencies
CF	concentration factor	solution concentration of cell e normalized to the influent concentration
X	mass	water mass in the maximally filled feed channel
V	velocity	feed velocity through the feed channel
A	area	cross-sectional area of the RO module
th	thickness	thickness of a module dimension
Q	volumetric flow	feed flow through a maximally filled feed channel
Δt	time	timestep of the simulation that adheres to the Courant condition
C_{max}	Courant constant	maximal value of the Courant constant to meet the Courant condition

continuation of Table 1

variable	name	description
ϕ	total concentration	total ionic concentrations in the simulation
C	specie concentration	concentration of an individual specie
v	stoichiometry coefficient	coefficient for the respective compound in the balanced equilibrium reaction
N	number of reactions	quantity of reactions that contain a respective compound
R	reaction flux	$\frac{mmol}{hour}$ flux of an equilibrium reaction
Ω	thermodynamic displacement	logarithm of the $\frac{Q_{dissolution}}{K_{sp}}$
k_m	rate constant	dissolution and precipitation rate constant
a	activity	chemical activity of the respective compound
η & p	parameter	experimentally determined parameter
ΔG	Gibbs free energy	Gibbs free energy of the dissolution and precipitation reactions
K	equilibrium constant	thermodynamic equilibrium of the respective reaction
M	number of minerals	quantity of minerals in the studied system
γ	activity coefficient	coefficient of metabolite activity in a respective system
z	charge	compound charge of the respective metabolite
μ	ionic strength	charge-weighted concentration of a solution
A & B	parameter	experimentally determined parameter

continuation of Table 1

variable	name	description
a_j & b_j	fitted parameter	geochemical parameter that is fit to the system
W_{aq}	water mass	mass of water in the system

2.2 Transport

Feed water is represented as a single solution that aggregates the bulk solution and the concentration polarization (CP)[63,64] that develops at the membrane surface as a consequence of the no-slip boundary condition.[65] The inlet boundary is defined as constant via the Dirichlet boundary condition,[66] where the influent feed is assumed to be an infinite reservoir whose characteristics are unaffected by the RO system. The outlet boundary is defined as changing with the Cauchy boundary condition,[67] where the effluent characteristics are a function of desalination. The membrane-feed interface of our model is discretized into $n \in \mathbb{W}$ cells that are an equal fraction of the total module length l_{module}. Each cell e simulates permeate flux as 100% water, similar to other RO models,[68] and as the change in moles ($\Delta\Phi_e$) of feed solution since the feed pressure P and osmotic pressure π[69] that govern permeate flux

$$\Delta\Phi_e \; \alpha \; (P - \pi), \tag{1}$$

are neither often experimentally measured nor reported.

2.2.1 Permeate Flux

The transport of permeate water ($\Delta\Phi_e$) is assumed to decrease exponentially along the RO module distance. The concentration change of a given point in the module relative to the

feed concentration is quantitatively tracked as the concentration factor (CF)

$$CF = \frac{initial}{final} \tag{2}$$

as the quotient of initial to final ionic concentrations (influent vs. effluent),[52] solution masses, or permeate moles. The slope of concentration change is calculated

$$slope_{CF} = \frac{CF_n - CF_1}{n}, \tag{3}$$

where the effluent CF_n is the average CF of all effluent ion concentrations

$$CF_n = \frac{\sum_{i=1}^{j}(C_{i,brine})}{\sum_{i=1}^{j}(C_{i,feed})}, \tag{4}$$

from the $C_{i,brine}$ effluent concentration and $C_{i,feed}$ influent concentration of ion i, for all j ions. Defining CF from eq. (2) in terms of moles of feed solution (Φ, 100% water) reveals an equation

$$CF_e = \frac{\Phi_0}{\Phi_e} = \frac{\Phi_0}{\Phi_0 - \Delta\Phi_{(1,e)}} \tag{5}$$

that can calculate the moles of feed at the end of an arbitrary cell e ($\Phi_e = \Phi_0 - \Delta\Phi_{(1,e)}$. The sum of permeate flux that occurred between cell 1 and the end of cell e

$$\Delta\Phi_{(1,e)} = \Delta\Phi_e + \Delta\Phi_{(1,e-1)} \tag{6}$$

is separately the sum of permeate flux before the start of cell e ($\Delta\Phi_{(1,e-1)} = \sum_{j=1}^{e-1}(\Delta\Phi_j)$) and the permeate flux over cell e ($\Delta\Phi_e$). The initial moles of feed Φ_0 is calculated

$$\Phi_0 = V_{feed} * MW_{H_2O} * \rho_{H_2O}, \tag{7}$$

from the volume of the feed channel V_{feed}, which is the product of the module length l_{module} and the cross-sectional area of the feed channel A_{feed}

$$A_{feed} = (A_{module} - A_{permeate}) * \frac{th_{feed}}{th_{unit}} \ , \tag{8}$$

where A_{module} and $A_{permeate}$ are the cross-sectional areas of the whole module and the permeate tube, respectively, and th_{feed} and th_{unit} are the thicknesses of the feed channel and the repeating membrane unit in Figure S1, respectively. The linear expression for CF_e

$$CF_e = (slope_{CF}) * e + CF_0 \ , \tag{9}$$

is then substituted into eq. (5), with the slope from eq. (3), to yield an expression for the permeate flux (a negative change in feed moles) at the end of each examined cell e

$$-\Delta\Phi_{(1,e)} = \frac{\Phi_0}{((\frac{CF_n - CF_0}{n}) * e + CF_0)} - \Phi_0 \ , \tag{10}$$

which can be substituted into eq. (6) to yield the permeate flux over any examined cell e ($\Delta\Phi_e$), analogously to **??**. Note that $\Delta\Phi_{(1,e-1)} = 0$ when $e = 1$, since there are no previous cells.

The calculation sequence for this permeate flux method is summarized:

1. Define the effluent CF
2. Calculate the feed capacity of the module [eqs. (7) and (8)]
3. Calculate the CF slope [eq. (3)]
4. Calculate the permeate flux in each cell [eqs. (5), (6), (9) and (10)]

2.2.2 Feed Flow

The migration of feed through the module is simulated through the following sequence with each timestep: 1) the contents of each cell e migrate to the next cell $e+1$; 2) cell 1 is repopulated; and 3) cell n is deleted. The feed velocity $v_{feed} = \frac{Q_{max\ feed}}{A_{feed}}$ is calculated from the maximum feed flowrate $Q_{max\ feed}$ ($\frac{m^3}{s}$) and the feed area from eq. (8) of the RO module. The maximum simulation timestep $\Delta t = \frac{l_{cell}}{v_{feed}}$ is calculated according to the Courant Condition[70] ($C_{max} = 1 \geq \frac{v_{feed} * t_{max}}{l_{cell}}$) to maintain accurate resolution of the feed flow.

2.3 Geochemistry

Our model leverages PHREEQC to qualitatively and quantitatively determine scaling and brine concentrations from the fundamental geochemical kinetic rate laws and thermodynamic equilibria of each mineral, and is receptive to feed conditions in every cell at each timestep. These chemical operations are exhaustively derived in version 3 of the PHREEQC manual,[71] and utilize the PHREEQC databases of chemical constants as parameters. These databases are processed for ROSSpy by our ChemW Python package that calculates the molecular mass of each inorganic formula (see the ChemW PyPI documentation), which were omitted in the databases but are necessary to quantitatively predict scaling in the conventional units of $\frac{g\ scale}{m^2\ membrane}$.

2.3.1 PHREEQ

The most pertinent calculations of PHREEQC for our model are summarized in the following sub-section, while the version 3 PHREEQC User's manual provides a rigorous description of all PHREEQC operations.

The total concentration Ψ_i of ionic species i is calculated in each timestep,

$$\Psi_i = C_i + \sum_{j=1}^{J} (v_{ij} * C_j), \tag{11}$$

where C_i is the molal concentration; J is the set of compounds that contain i; C_j is the molal concentration of compound j; and v_{ij} is the stoichiometric coefficient for the moles of i per mole of compound j. Mineral equilibria over the t timestep is calculated through a similar equation,

$$\frac{\partial \Psi_i}{\partial t} = \sum_{m=1}^{N_m} (v_{mj} * R_m), \tag{12}$$

where N_m is the set of reactions that include specie i; v_{mj} is the stoichiometric coefficient for the moles of i per mole of mineral m; and R_m is the reaction flux of dissolution or precipitation for $(+)$ and $(-)$, respectively,

$$R_m = sgn[\Omega] * A_m * k_m * (\Pi(a^n))|e^{\frac{\eta * \Delta G}{RT}} - 1|^p, \tag{13}$$

where $\Omega = log\left(\frac{Q_{dissolution}}{K_{sp}}\right)$ and, for the simulated mineral m, A_m is the reacting surface area; k_m is the rate constant of dissolution or precipitation; Q_m is the ion activity product constant; and η and p are experimentally determined parameters. The $|e^{\frac{\eta * \Delta G}{RT}} - 1|^p$ term simplifies to 1 for irreversible precipitation or dissolution. The set of eqs. (11) and (12) necessitates that any perturbations to ionic concentrations $\frac{\partial \Psi_i}{\partial t}$ manifest from complexation equilibria. The molal concentration C_j of compound j is discerned,

$$C_j = \frac{\Pi_{j=1}^{N_c} (\gamma_j * K_j)^{v_{ij}}}{\gamma_j * K_j}, \tag{14}$$

where N_c is the set of linearly independent chemical reactions; γ_j is the activity coefficient of compound j; and K_j is the equilibrium constant

$$K_j = a_j \Pi_m^{M_{aq}} (a_m)^{-v_{m,j}}, \tag{15}$$

where M_{aq} is the number of minerals in the aqueous system; $v_{m,i}$ is the stoichiometric coefficient of compound j per mole of mineral m; and a_j and a_m are the activity coefficients of compound j and mineral m, respectively. The activity coefficient γ_j is calculated through

either the Debye-Hückel model,[72]

$$log(\gamma_j) = -A * z_j^2 \sqrt{\mu}, \tag{16}$$

the WATEQ Debye-Hückel model,[72]

$$log(\gamma_j) = \frac{-A * z_j^2 * \sqrt{\mu}}{1 + B * a_j^0 * \sqrt{\mu}} + b_j \mu, \tag{17}$$

the Davies model,[73]

$$log(\gamma_j) = -A * z_j^2 (\frac{\sqrt{\mu}}{1 + \sqrt{\mu}} - 0.2\mu), \tag{18}$$

or the empirical Pitzer model,[74] where A and B are experimentally determined parameters; a_j^0 and b_j are fitted parameters; z_j is the charge of compound j; and μ is the ionic strength of the solution

$$\mu = \frac{1}{2} \sum_{j=1}^{N_{aq}} z_j^2 \frac{n_j}{W_{aq}}, \tag{19}$$

where W_{aq} is the simulated water mass and n_j

$$n_j = C_j * W_{aq} = \frac{K_i * W_{aq}}{\gamma_j * (\Pi_m^{M_{aq}} (a_m)^{v_{m,j}}} \tag{20}$$

is the moles of compound j. These calculations and geochemical models are more thoroughly described in the PHREEQC manual and in the cited literature.

2.3.1 Brine concentrations

The effluent brine concentrations are estimated by applying the CF to the influent feed concentrations for each respective ion.

3 Results and Discussion

The following sub-sections demonstrate the features of our model and its alignment with reported measurements. These studies were conducted through ROSSpy and are available as Python Notebooks in the ROSSpy GitHub repository.

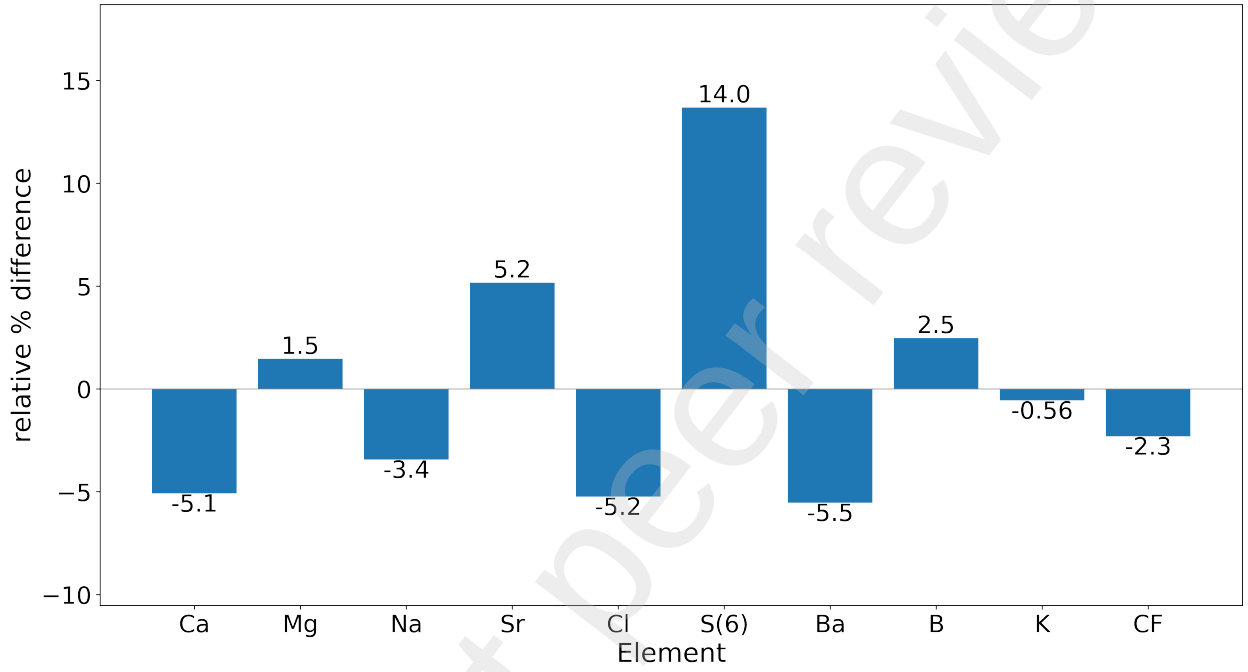

(a) Prediction %-errors to Zaman et al.[56] experimental data

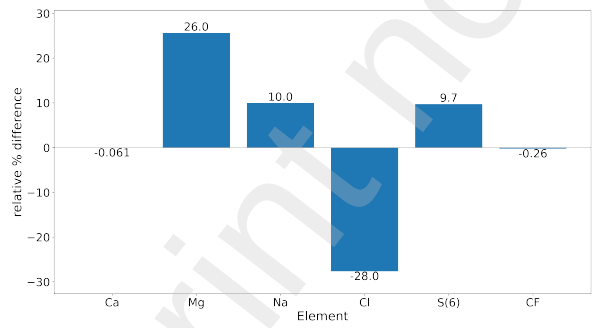

(b) Prediction %-errors to Hajbi et al.[58] data

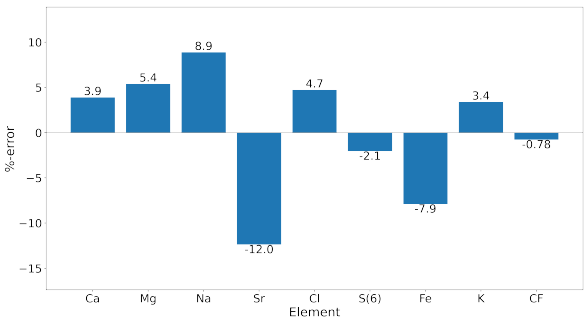

(c) Prediction %-errors to Ahmed et al.[57] data

Figure 1: The %-error between predicted brine concentrations and experimental concentrations from a few experimental studies. The comparisons are illustrated with different y-axis scales to optimize resolution of the bars. Prediction accuracy seems to be proportional with the quantity of parameterized ions and other geochemical parameters, which intuitively supports that more data improves simulation results.

3.1 CF and Brine formation

The predicted CF and ionic concentrations of the effluent were verified through comparisons with the following three experimental studies, where the reported feed geochemistry and module specifications were parameterized into the model.

3.1.1 Zaman et al.[56]

This study examines RO brine, from a full-scale water treatment facility in Australia, to understand which minerals are likely to form as scale. The predicted concentrations in Figure 1 were $< 6\%$-error relative to the experimental concentrations for all but one of the feed ions.

3.1.2 Ahmed et al.[57]

This study examines RO brine from 10 small desalination plants in Oman and 8 plants in the United Arab Emirates (UAE) for the purpose of understanding ideal brine disposal methods. We selected the UAE Qidfa I desalination plant, since it provided the most comprehensive experimental details. The predicted concentrations in Figure 1 were $< 10\%$-error for all but one of the feed ions. The CF, in the far-right column of Figure 1, exhibits a $< 1\%$-error relative to experimental measurements which supports that the reactive transport processes, notably the representation of permeate flux, are accurate and that error is mostly attributed to the geochemical calculations.

3.1.3 Hajbi et al.[58]

This study evaluates the recovery of commodity salts from RO brine at a plant in Tunisia. The authors detail feed geochemistry and specifications of line D – a polyamide filtration membrane – in the plant system, which were both parameterized into our model. The predicted concentrations in Figure 1 were less aligned than the aforementioned two studies, with two ions exceeding 25%-error, which is attributed to this study defining 3-4 fewer feed

ions and therefore describes an incomplete geochemical description of the system that skews calculations and results. The variability among the ions, however, appears to neutralize since the CF prediction in Figure 1 maintains accuracy.

3.2 Scaling

The scaling predictions were verified qualitatively from experimental literature and quantitatively from the following theoretical calculations of solubility thermodynamics, since experimental literature that quantified feed geochemistry and observed scalants was not available.

3.2.1 Quantitative The quantitative verification consisted of two simple cases of Gypsum precipitation. 1) A simple solution of only Ca^{2+} and SO_4^{2-} was predicted to precipitate gypsum within 5% of the observed change in ionic concentrations (Table **??**). This 5% discrepancy in mass balance is attributed to the printed PHREEQC values in this calculation neglecting diffusion within the feed solution, yet diffusion is considered in the final output of PHREEQC. 2) Gypsum precipitation from desalinating the simple solution of (1) is juxtaposed with that from desalinating our geochemical representation of the Red Sea. This comparison assesses the consistency of scaling in simple and complex feed solutions. The simple solution precipitated 7% fewer moles of Gypsum compared to the Red Sea (Table S1), which is attributed to ionic interactions within the complex Red Sea feed that are not present in the simple solution of only Ca^{2+} and SO_4^{2-} ions. These subtle $[5, 7]\%$ deviations, notwithstanding the coarseness of the simple feed solution, are relatively minor in the context of other sources of error, such as feed measurements, and suggest that our model is quantitatively consistent with expected scaling.

The scaling predictions were qualitatively verified through the following three experimental studies.

Karabelas et al., 2020[59] This study inspired features of ROSSpy by reviewing the state-of-the-art, and future directions, for predictive scaling software. The Supporting Information of this study also, importantly, describes scalants after desalination with defined feed conditions. These scalants were reported as including "Calcite but not Gypsum" and a "few other salts, such as Barite and Dolomite, could also deposit at downstream...". Scaling predictions from our model with these conditions in Figure 2(a) match the reported scalants in numerous aspects: 1) Calcite was the primary scalant; 2) Gypsum was not observed; 3) a few other salts precipitated, including Dolomite and Barite, depending upon the PHREEQC database; and 4) these other salts precipitated primarily in the downstream portion of the module.

Karabelas et al., 2014[60] This study investigated the mechanisms of incipient scaling from RO desalination, with Gypsum as the example scalant.[75] The most thoroughly described trial from the experiment (28SC) was simulated and Gypsum was the only predicted scalant in Figure 2(b), just as the study reported.

Lee et al., 2009[61] This study evaluates the use of a membrane bioreactor – a hollow-fiber membrane module design that is mechanistically similar to RO – to treat wastewater. The wastewater filtration system was simulated, and the only predicted scalant was Calcite in Figure 2(c), just as the study reported.

3.3 Applications

3.3.1 Feed Sources

We examined numerous potential feed souced based on experimental geochemical literature for the respective sources, including both natural seas and produced waters from oil wells. A sampling of these feed sources was simulated in Figure 3. The scaling and brine predictions differed significantly amongst these feed water sources, which suggests that feed geochemistry

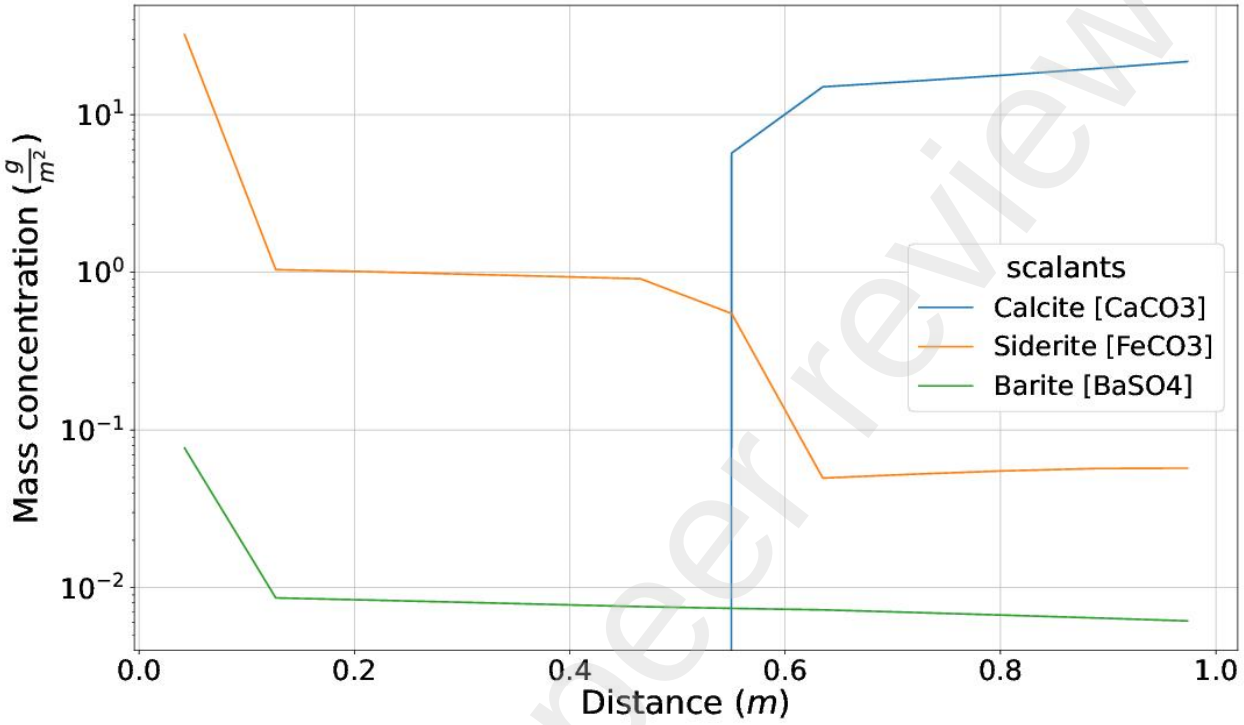

(a) Scaling predictions when parameterizing the Karabelas et al., 2020 experimental data

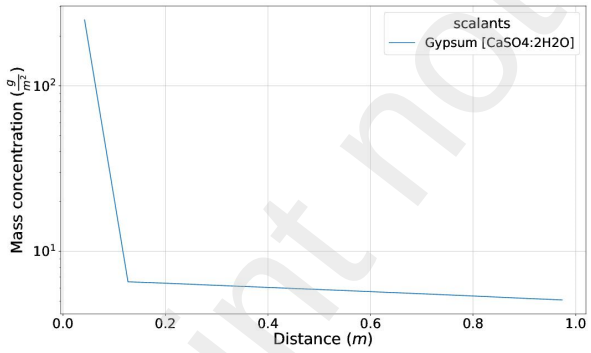

(b) Scaling predictions of the Karabelas et al., 2014 data

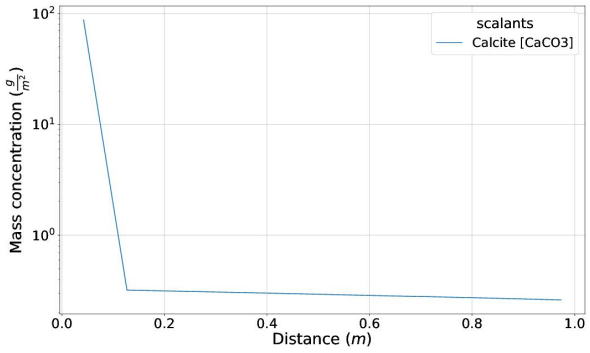

(c) Scaling predictions of the Lee et al., 2009 data

Figure 2: The qualitative scaling predictions from data of a few experimental studies. Alignment of these predictions with the qualitative descriptions from the respective studies contributed part of the experimental validation of the scaling predictions from our model.

should be carefully curated before simulation to avoid variability of pollution,[76] seasonality,[77] or incompatible assumptions from different data sources. We propose experimental literature of numerous other water sources in the Supporting Information that can be curated into parameters for simulation through our model.

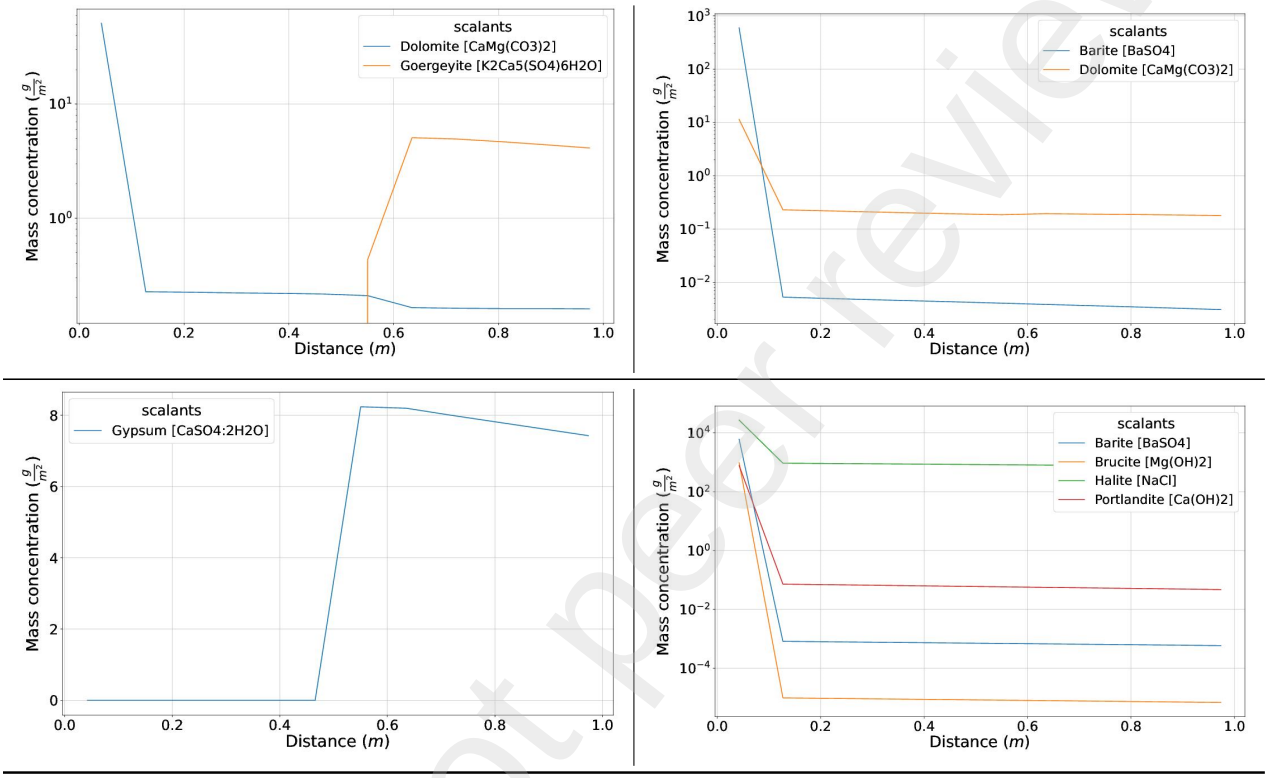

Figure 3: Scaling predictions of (clockwise from top left) experimentally defined feed waters of the Mediterranean Sea, produced waters from the Palo Duro oil basin, produced waters from the North German oil basin, and the Red Sea. These subfigures sample the diversity of scaling predictions from varied feed sources, and exhibit a high sensitivity of scale predictions to the feed geochemistry.

3.3.2 Database selection

The selection of a PHREEQC database 1) determines the set of minerals that can potentially scale; 2) governs scaling through the kinetic, thermodynamic, and stoichiometric descriptions of each mineral precipitation/dissolution reaction; and 3) employs a chemical activity model to calculate feed saturation: e.g. the Pitzer, Debye-Hückel, and Davies models. The Pitzer model,[74] which is implemented in the *pitzer.dat* PHREEQC database, is more accurate in

the concentration range of solutions that are typically encountered during desalination;[78,79] however, the limited availability of geochemical data for numerous ions and minerals may require using other databases, such as wateq4, for complex or uncommon feed sources.

Each of the 13 databases were simulated in desalinating the Red Sea. The *Amm*, *Core*10, *LLNL*, and *Minteq.v*4 databases failed to converge, while the other 9 databases generated scaling predictions that are summarized in Figure 4. The comparison of predictions indicates that the database selection substantially influences scaling results, and thus should be carefully selected.

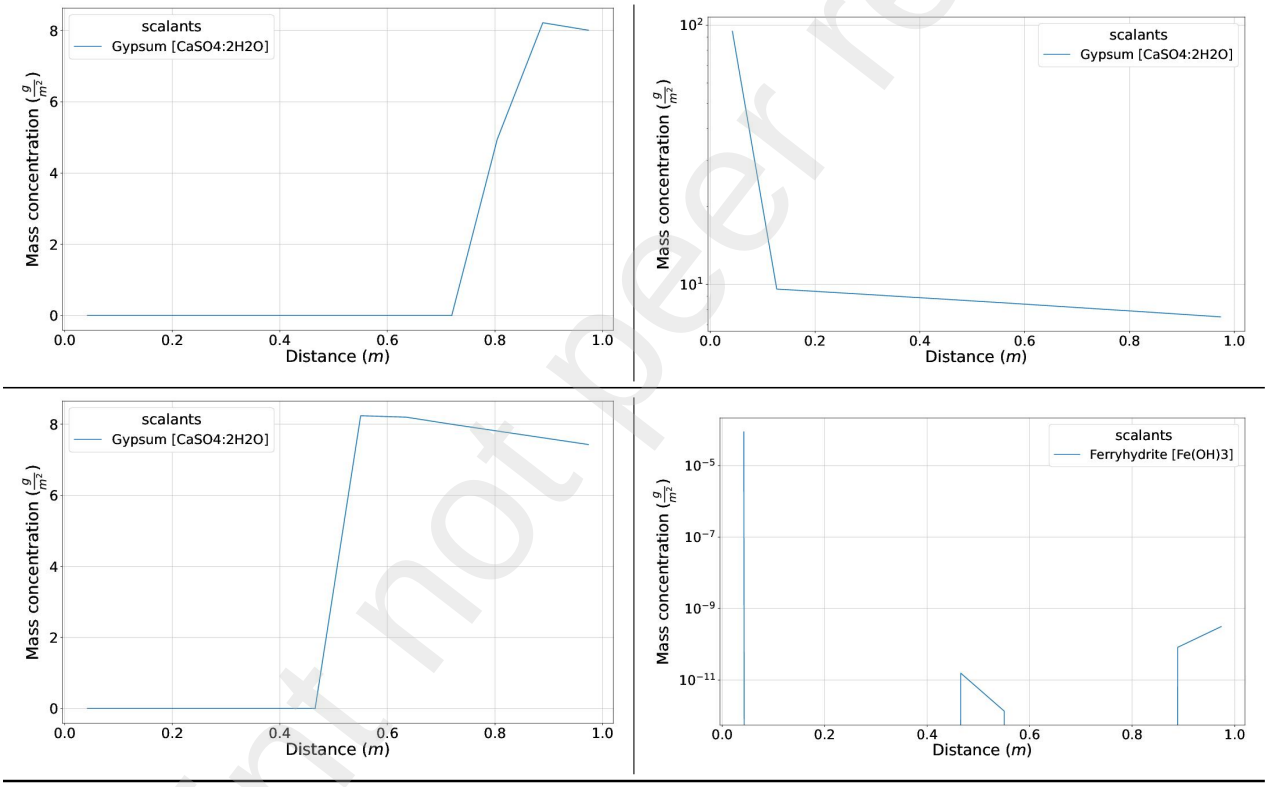

Figure 4: Scaling predictions from (clockwise from top left) the ColdChem, Iso, Sit, and Pitzer databases, with otherwise identical simulation parameters. These subfigures sample the diversity of scaling predictions by parameterizing different PHREEQC databases, which exemplifies that the PHREEQC database should be deliberately selected to best capture the simulated feed geochemistry.

3.4 Sensitivity Analyses

A few sensitivity analyses were conducted with major variables and parameters of our model in the following subsections. Additional sensitivity analyses of lesser parameters are presented in the Supporting Information.

Feed geochemistry

Feed source geochemistry influences RO operation[80] and therefore are important to capture with our model.

3.5 ROSSpy Software

ROSSpy, which is conceptually embodied in Figure 5, combines our one-dimensional RO model with post-processing operations that facilitate interpretation of the simulation results. The software a) translates parameters into a PHREEQ input file; b) executes that input file via PHREEQpy; c) processes the simulation results into figures and data tables via Matplotlib[81] and Pandas[82] Python packages, respectively; and d) exports all of the simulation content – e.g. the PHREEQ input file, SVG data figures, and CSV files of parameters, variables, data, and brine predictions – into a specified folder and directory. The simulation data may be sliced into one-dimensional sets of distance or time that can be plotted against either scaling density or brine concentrations (Figures S2-S3) (see ROSSpy documentation).

4. Conclusion

A light-weight model of scaling during RO desalination that coalesces the geochemical rigor of PHREEQC and the elegant simplicity of one-dimensional transport has been derived and demonstrated. This practical tool resolved the spatiotemporal dynamics of desalination scaling and demonstrated accuracy for the diverse brackish feedwaters that were validated via both geochemical theory and experimental data where it was available. The API implemen-

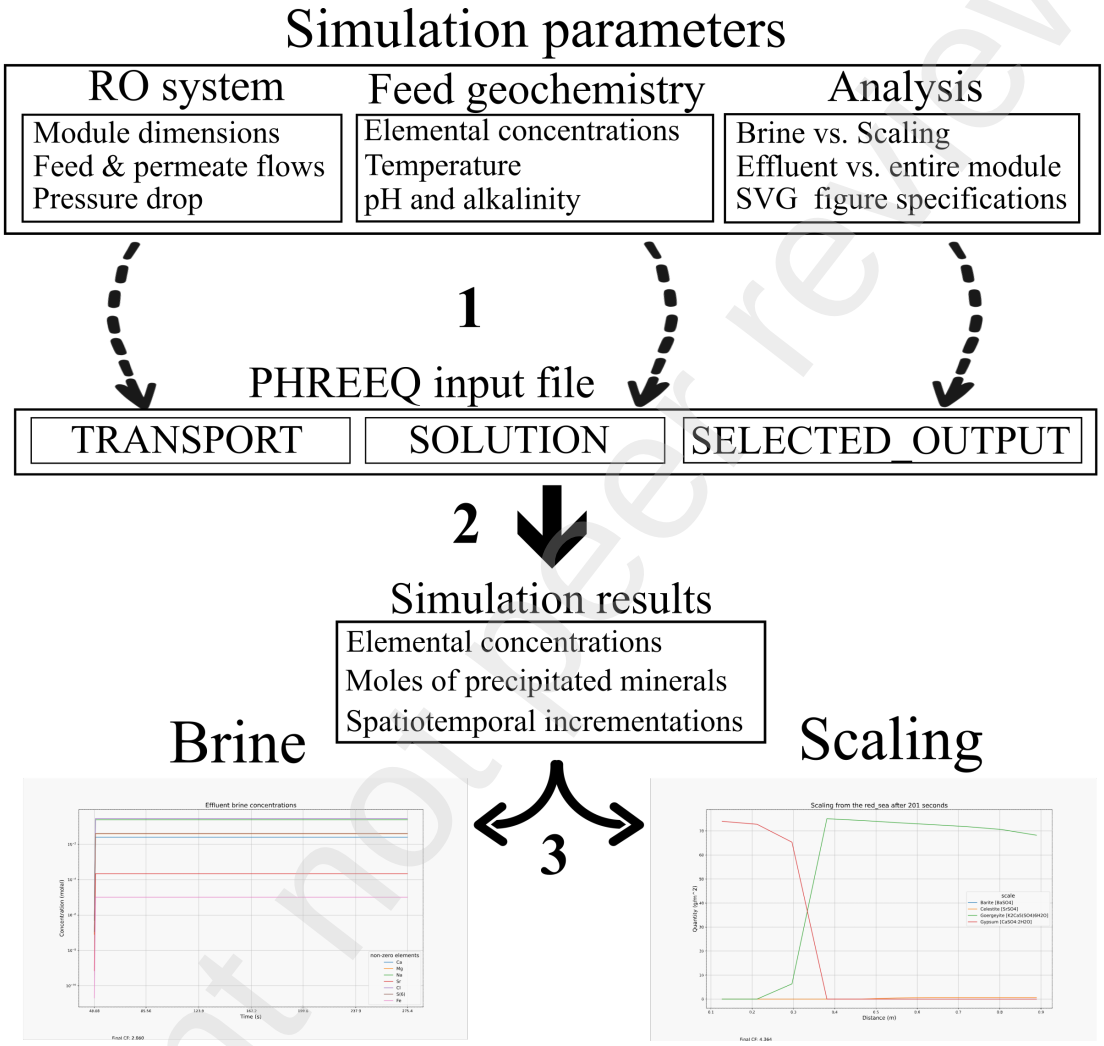

Figure 5: The ROSSpy workflow. Step 1 describes the translation of parameters – i.e. module specifications, feed geochemistry, and simulation analysis – into the corresponding code blocks of a PHREEQ input file. Step 2 describes executing the PHREEQ input file to acquire simulation results. Step 3 describes processing the simulation results into predictions of scaling or brine concentrations that are expressed as figures and datatables.

tation of this model (ROSSpy) furthermore meets identified needs of the community – e.g. rapidly designing, executing, processing, and exporting simulations of RO scaling – while maintaining accessibility through its computationally efficient and open-source code. The model has no concept of antiscalants, since the model is intended to resolve scaling from native feedwaters and not optimize for antiscalant treatments, but this may be an advantageous next addition to the model and ROSSpy. We expect that this model and API will may find a niche for preliminary analysis of the scaling outcomes for various feed conditions and RO modules. Computational tools such as our model will be imperative in innovating new RO modules and feed systems that can mitigate scaling and ultimately alleviate the accenuating concern of chronic water insecurities across the world.

5. Funding

This work was prepared in partial fulfillment of the requirements of the Berkeley Lab Undergraduate Research (BLUR) Program, managed by Workforce Development & Education at the Berkeley Lab. The project was also partly funded by NSERC Discovery, MITACS Accelerate, CEWIL, and Canada Summer Jobs.

Acknowledgement

The authors thank Ethan Sean Chan for his technical assistance in developing a forthcoming interactive version of ROSSpy (iROSSpy). The authors additionally thank Nusret Ipek, Min Yang, and Lixuan An for invaluable feedback that improved the accessibility of ROSSpy software.

Supporting Information Available

A complete Supporting Information document is associated with this paper. All of the described simulation figures and experiments are presented in the examples folder of the ROSSpy GitHub page `https://github.com/freiburgermsu/ROSSpy`.

References

(1) Hoekstra, A. Y.; Mekonnen, M. M.; Chapagain, A. K.; Mathews, R. E.; Richter, B. D. Global monthly water scarcity: Blue water footprints versus blue water availability. *PLoS ONE* **2012**, *7*.

(2) Laghari, J. Melting glaciers bring energy uncertainty. *Nature* **2013**, *502*, 617–618.

(3) Rasul, G.; Dahe, Q.; Chaudhry, Q. Z. Global Warming and Melting Glaciers along Southern Slopes of HKH Ranges. *Pakistan Journal of Meteorology* **2008**, *5*, 63–76.

(4) Shiklomanov, I. A. *Water in Crisis: A guide to the world's fresh water resources*; Oxford University Press, 1993; Chapter 2, pp 13–24.

(5) Hansen, J.; Sato, M.; Ruedy, R.; Lo, K.; Lea, D. W.; Medina-Elizade, M. Global temperature change. *Proceedings of the National Academy of Sciences of the United States of America* **2006**, *103*, 14288–14293.

(6) Thomas, C. D. et al. Extinction risk from climate change. *Nature* **2004**, *427*, 145–148.

(7) Meyer, W. B.; Turner II, B. L. Human population growth and global land-use/cover change. *Annual Review of Ecology and Systematics* **1992**, *23*, 39–61.

(8) Möller, A.; Ahrens, L.; Surm, R.; Westerveld, J.; Van Der Wielen, F.; Ebinghaus, R.; De Voogt, P. Distribution and sources of polyfluoroalkyl substances (PFAS) in the River Rhine watershed. *Environmental Pollution* **2010**, *158*, 3243–3250.

(9) Jones, E.; Qadir, M.; van Vliet, M. T.; Smakhtin, V.; Kang, S. m. The state of desalination and brine production: A global outlook. *Science of the Total Environment* **2018**, *657*, 1343–1356.

(10) Service, R. F. Desalination Freshens Up. *Science* **2006**, *313*, 1088–1090.

(11) Amy, G.; Ghaffour, N.; Li, Z.; Francis, L.; Linares, R. V.; Missimer, T.; Lattemann, S. Membrane-based seawater desalination: Present and future prospects. *Desalination* **2017**, *401*, 16–21.

(12) Malaeb, L.; Ayoub, G. M. Reverse osmosis technology for water treatment: State of the art review. *Desalination* **2011**, *267*, 1–8.

(13) Karime, M.; Bouguecha, S.; Hamrouni, B. RO membrane autopsy of Zarzis brackish water desalination plant. *Desalination* **2008**, *220*, 258–266.

(14) Hafez, A.; El-Manharawy, S. Economics of seawater RO desalination in the Red Sea region, Egypt. Part 1. A case study. *Desalination* **2003**, *153*, 335–347.

(15) Shemer, H.; Semiat, R. Sustainable RO desalination – Energy demand and environmental impact. *Desalination* **2017**, *424*, 10–16.

(16) Council, U.-S. B. Water in Saudi Arabia: Desalination, Wastewater, and Privatization. 2021; `https://ussaudi.org/water-in-saudi-arabia-desalination-wastewater-and-privatization/`.

(17) Jeppesen, T.; Shu, L.; Keir, G.; Jegatheesan, V. Metal recovery from reverse osmosis concentrate. *Journal of Cleaner Production* **2009**, *17*, 703–707.

(18) Mavukkandy, M. O.; Chabib, C. M.; Mustafa, I.; Al Ghaferi, A.; AlMarzooqi, F. Brine management in desalination industry: From waste to resources generation. *Desalination* **2019**, *472*, 114187.

(19) Allen, J. C. Process for recovering iodine from oil well brine. 1954.

(20) Flemming, H.-C. Reverse Osmosis Membrane Biofouling. 1997; https://scholar.google.com/scholar?as_vis=0&q=reverse+osmosis+membrane+technology+amjad+ed&hl=en&as_sdt=0,47.

(21) Cantor, P. A.; Mechalas, B. J. Biological degradation of cellulose acetate reverse-osmosis membranes. *Journal of Polymer Science Part C: Polymer Symposia* **1969**, *28*, 225–241.

(22) Ivnitsky, H.; Katz, I.; Minz, D.; Shimoni, E.; Chen, Y.; Tarchitzky, J.; Semiat, R.; Dosoretz, C. G. Characterization of membrane biofouling in nanofiltration processes of wastewater treatment. *Desalination* **2005**, *185*, 255–268.

(23) Warsinger, D. M.; Swaminathan, J.; Guillen-Burrieza, E.; Arafat, H. A.; Lienhard V, J. H. Scaling and fouling in membrane distillation for desalination applications: A review. *Desalination* **2015**, *356*, 294–313.

(24) Khan, M. T.; Manes, C. L. d. O.; Aubry, C.; Croué, J. P. Source water quality shaping different fouling scenarios in a full-scale desalination plant at the Red Sea. *Water Research* **2013**, *47*, 558–568.

(25) Tang, F.; Hu, H. Y.; Sun, L. J.; Wu, Q. Y.; Jiang, Y. M.; Guan, Y. T.; Huang, J. J. Fouling of reverse osmosis membrane for municipal wastewater reclamation: Autopsy results from a full-scale plant. *Desalination* **2014**, *349*, 73–79.

(26) Shmulevsky, M.; Li, X.; Shemer, H.; Hasson, D.; Semiat, R. Analysis of the onset of calcium sulfate scaling on RO membranes. *Journal of Membrane Science* **2017**, *524*, 299–304.

(27) Goosen, M. F.; Sablani, S. S.; Al-Hinai, H.; Al-Obeidani, S.; Al-Belushi, R.; Jackson, D. Fouling of reverse osmosis and ultrafiltration membranes: A critical review. *Separation Science and Technology* **2004**, *39*, 2261–2297.

(28) Elimelech, M.; Phillip, W. A. The future of seawater desalination: Energy, technology, and the environment. *Science* **2011**, *333*, 712–717.

(29) Ye, M.; Pasta, M.; Xie, X.; Dubrawski, K. L.; Xu, J.; Liu, C.; Cui, Y.; Criddle, C. S. Charge-Free Mixing Entropy Battery Enabled by Low-Cost Electrode Materials. 2019.

(30) Matin, A.; Rahman, F.; Shafi, H. Z.; Zubair, S. M. Scaling of reverse osmosis membranes used in water desalination: Phenomena, impact, and control; future directions. *Desalination* **2019**, *455*, 135–157.

(31) Alshami, A.; Taylor, T.; Ismail, N.; Buelke, C.; Schultz, L. RO system scaling with focus on the concentrate line: Current challenges and potential solutions. *Desalination* **2021**, *520*, 115370.

(32) Ruiz-García, A.; Feo-García, J. Antiscalant cost and maximum water recovery in reverse osmosis for different inorganic composition of groundwater. EDS Conference on Desalination for the Environment: Clean Water and Energy. 2016; pp 46–53.

(33) Hu, Y.; Xu, Y.; Xie, M.; Huang, M.; Chen, G. Characterization of scalants and strategies for scaling mitigation in membrane distillation of alkaline concentrated circulating cooling water. *Desalination* **2022**, *527*, 115534.

(34) Ruiz-García, A.; Nuez, I.; Carrascosa-Chisvert, M. D.; Santana, J. J. Simulations of BWRO systems under different feedwater characteristics. Analysis of operation windows and optimal operating points. *Desalination* **2020**, *491*, 114582.

(35) Hu, Z.; Antony, A.; Leslie, G.; Le-Clech, P. Real-time monitoring of scale formation in reverse osmosis using electrical impedance spectroscopy. *Journal of Membrane Science* **2014**, *453*, 320–327.

(36) Cheng, Z.; Qin, Q.; Jia, H.; Li, J.; Yan, F.; Meng, X.; Wang, J. Scale evaluation and

antiscalant testing based on fluorescent probe technology in RO process. *Journal of Membrane Science* **2021**, *636*, 119598.

(37) Bouchareb, A.; Metaiche, M.; Lounici, H. Experimental versus theoretical study of reverse osmosis pilot scaling: The case of Algerian brackish water desalination. *Journal of Water and Land Development* **2019**, *42*, 49–58.

(38) Najid, N.; Hakizimana, J. N.; Kouzbour, S.; Gourich, B.; Ruiz-García, A.; Vial, C.; Stiriba, Y.; Semiat, R. Fouling control and modeling in reverse osmosis for seawater desalination: A review. *Computers and Chemical Engineering* **2022**, *162*, 107794.

(39) *Zero Brine D2 . 1 Modelling a brine regeneration cycle using PHREEQC*; 2018.

(40) Desalitech, ROSA membrane projection software. `https://www.desalitech.com/rosa_download_lp/`.

(41) Walker, P.; Sheikholeslami, R. Assessment of the effect of velocity and residence time in CaSO4 precipitating flow reaction. *Chemical Engineering Science* **2003**, *58*, 3807–3816.

(42) Steefel, C. I. et al. Reactive transport codes for subsurface environmental simulation. *Computational Geosciences* **2015**, *19*, 445–478.

(43) Kundu, P. *Technical basis for OLI membrane technology*; 2018.

(44) Radu, A. I.; Bergwerff, L.; van Loosdrecht, M. C.; Picioreanu, C. A two-dimensional mechanistic model for scaling in spiral wound membrane systems. *Chemical Engineering Journal* **2014**, *241*, 77–91.

(45) Karabelas, A. J.; Mitrouli, S. T.; Koutsou, C. P.; Kostoglou, M. Prediction of spatial-temporal evolution of membrane scaling in spiral wound desalination modules by an advanced simulator. *Desalination* **2019**, *458*, 34–44.

(46) Software, F. C. Reverse Osmosis. `https://www.frenchcreeksoftware.com/`.

(47) Strubbe, L. Calibration of a Reverse Osmosis Model At Full-Scale. **2018**,

(48) Mitrouli, S. T.; Kostoglou, M.; Karabelas, A. J. Calcium carbonate scaling of desalination membranes: Assessment of scaling parameters from dead-end filtration experiments. *Journal of Membrane Science* **2016**, *510*, 293–305.

(49) Warsinger, D. M.; Tow, E. W.; Maswadeh, L. A.; Connors, G. B.; Swaminathan, J.; Lienhard V, J. H. Inorganic fouling mitigation by salinity cycling in batch reverse osmosis. *Water Research* **2018**, *137*, 384–394.

(50) Bein, A.; Dutton, A. R. Origin, distribution, and movement of brine in the Permian Basin (U.S.A.): A model for displacement of connate brine. *Geological Society of America Bulletin* **1993**, 695–707.

(51) Wilson, T. P.; Long, D. T. Geochemistry and isotope chemistry of Michigan Basin brines: Devonian formations. *Applied Geochemistry* **1993**, *8*, 507–524.

(52) Casas, S.; Aladjem, C.; Cortina, J. L.; Larrotcha, E.; Cremades, L. V. Seawater Reverse Osmosis Brines as a New Salt Source for the Chlor-Alkali Industry: Integration of NaCl Concentration by Electrodialysis. *Solvent Extraction and Ion Exchange* **2012**, *30*, 322–332.

(53) Yan, Z.; Yang, H.; Qu, F.; Yu, H.; Liang, H.; Li, G.; Ma, J. Reverse osmosis brine treatment using direct contact membrane distillation: Effects of feed temperature and velocity. *Desalination* **2017**, *423*, 149–156.

(54) WaterTAP contributors, WaterTAP: An open-source water treatment model library. Version 0.6.

(55) Wijmans, J. G.; Baker, R. W. The solution-diffusion model: a review. *Journal of Membrane Science* **1995**, *107*, 1–21.

(56) Zaman, M.; Birkett, G.; Pratt, C.; Stuart, B.; Pratt, S. Downstream processing of reverse osmosis brine: Characterisation of potential scaling compounds. *Water Research* **2015**, *80*, 227–234.

(57) Ahmed, M.; Shayya, W. H.; Hoey, D.; Al-Handaly, J. Brine disposal from reverse osmosis desalination plants in Oman and the United Arab Emirates. *Desalination* **2001**, *133*, 135–147.

(58) Hajbi, F.; Hammi, H.; M'Nif, A. Reuse of RO desalination plant reject brine. *Journal of Phase Equilibria and Diffusion* **2010**, *31*, 341–347.

(59) Karabelas, A. J.; Mitrouli, S. T.; Kostoglou, M. Scaling in reverse osmosis desalination plants: A perspective focusing on development of comprehensive simulation tools. *Desalination* **2020**, *474*, 114193.

(60) Karabelas, A. J.; Karanasiou, A.; Mitrouli, S. T. Incipient membrane scaling by calcium sulfate during desalination in narrow spacer-filled channels. *Desalination* **2014**, *345*, 146–157.

(61) Lee, M.; Kim, J. Membrane autopsy to investigate CaCO3 scale formation in pilot-scale, submerged membrane bioreactor treating calcium-rich wastewater. *Journal of Chemical Technology and Biotechnology* **2009**, *84*, 1397–1404.

(62) Charlton, S. R.; Parkhurst, D. L. Modules based on the geochemical model PHREEQC for use in scripting and programming languages. *Computers and Geosciences* **2011**, *37*, 1653–1663.

(63) Sablani, S.; Goosen, M.; Al-Belushi, R.; Wilf, M. Concentration polarization in ultrafiltration and reverse osmosis: A critical review. *Desalination* **2001**, *141*, 269–289.

(64) Zydney, A. L. Stagnant film model for concentration polarization in membrane systems. *Journal of Membrane Science* **1997**, *130*, 275–281.

(65) Rapp, B. E. *Microfluidics: Modeling, Mechanics and Mathematics*; ScienceDirect, 2017; Chapter 9, pp 273–276.

(66) Moës, N.; Béchet, E.; Tourbier, M. Imposing Dirichlet boundary conditions in the extended finite element method. *International Journal for Numerical Methods in Engineering* **2006**, *67*, 1641–1669.

(67) Gosses, M.; Nowak, W.; Wöhling, T. Explicit treatment for Dirichlet, Neumann and Cauchy boundary conditions in POD-based reduction of groundwater models. *Advances in Water Resources* **2018**, *115*, 160–171.

(68) Li, M. Optimal plant operation of brackish water reverse osmosis (BWRO) desalination. *Desalination* **2012**, *293*, 61–68.

(69) Lonsdale, H. K.; Merten, U.; Riley, R. L. Transport properties of cellulose acetate osmotic membranes. *Journal of Applied Polymer Science* **1965**, *9*, 1341–1362.

(70) Gnedin, N. Y.; Semenov, V. A.; Kravtsov, A. V. Enforcing the Courant–Friedrichs–Lewy condition in explicitly conservative local time stepping schemes. *Journal of Computational Physics* **2018**, *359*, 93–105.

(71) Parkhurst, D. L.; Appelo, C. A. L. *Description of input and examples for PHREEQC version 3: a computer program for speciation, batch-reaction, one-dimensional transport, and inverse geochemical calculations*; 2013.

(72) Aqion, Activity Coefficients (Activity Models). 2016; `https://www.aqion.de/site/101`.

(73) Davies, C. W. The extent of dissolution of salts in water_Part VIII. An equation for the mean ionic acitivity coefficient of an electrolyte in water, and a revision of the dissociation constants of some sulphates. *The Royal Society of Chemistry* **1938**, *0*, 2093–2098.

(74) Pitzer, K. S. Thermodynamics of electrolytes. I. Theoretical basis and general equations. *Journal of Physical Chemistry* **1973**, *77*, 268–277.

(75) Lyster, E.; Au, J.; Rallo, R.; Giralt, F.; Cohen, Y. Coupled 3-D hydrodynamics and mass transfer analysis of mineral scaling-induced flux decline in a laboratory plate-and-frame reverse osmosis membrane module. *Journal of Membrane Science* **2009**, *339*, 39–48.

(76) Chen, Y.; Paytan, A.; Chase, Z.; Measures, C.; Beck, A. J.; Sañudo-Wilhelmy, S. A.; Post, A. F. Sources and fluxes of atmospheric trace elements to the Gulf of Aqaba, Red Sea. *Journal of Geophysical Research* **2008**, *113*, 1–13.

(77) Sarthou, G.; Jeandel, C. Seasonal variations of iron concentrations in the Ligurian Sea and iron budget in the Western Mediterranean Sea. *Marine Chemistry* **2001**, *74*, 115–129.

(78) Sheikholeslami, R. Assessment of the scaling potential for sparingly soluble salts in RO and NF units. *Desalination* **2004**, *167*, 247–256.

(79) Mohammad, A. W.; Hilal, N.; Al-Zoubi, H.; Darwish, N. A. Prediction of permeate fluxes and rejections of highly concentrated salts in nanofiltration membranes. *Journal of Membrane Science* **2007**, *289*, 40–50.

(80) Van Wagner, E. M.; Sagle, A. C.; Sharma, M. M.; Freeman, B. D. Effect of crossflow testing conditions, including feed pH and continuous feed filtration, on commercial reverse osmosis membrane performance. *Journal of Membrane Science* **2009**, *345*, 97–109.

(81) Hunter, J. D. Matplotlib: A 2D graphics environment. *Computing in Science and Engineering* **2007**, *9*, 99–104.

(82) McKinney, W. *Pandas: a foundational Python library for data analysis and statistics*; 2011.

Supporting Information

Contents

List of Figures

List of Tables

1 ROSSpy

The variables and terms that comprise our model are defined in Table **??**. The distinctions between slicing the simulation data through time or module distance is exhibited with brine in Figure S1 and scaling in Figure S2, respectively.

Comparison of permeate flux methods Scaling predictions from these two permeate flux methods are juxtaposed in Figure S3. The most significant difference is observed at the module mid-point ($0.47m$), where the linear CF method predicts $0.99\frac{gram}{m^2}$ of Gypsum scale while the linear permeate flux method predicts $0.0196\frac{gram}{m^2}$ of Gypsum scale. The linear CF method after this mid-point predicts subtly less scale than the linear permeate method, as the exponential CF curve of the linear permeate method surpasses the linear CF curve from the linear CF method. This reinforces that scaling is determined by the feed CF. The total quantity of scale from these two methods equate $38.7\frac{gram}{m^2}$, however, which suggests that these methods only subtly affect the distribution, and not the total quantity, of scale. Experimental literature is not known that can verify which method better reflects physical systems.

2 PHREEQC consistency

	Ca^{2+}	+	SO_4^{2-}	$\leftrightharpoons$	$CaSO_4$
I	0.003913		0.00633		0
C	$-x$		$-x$		$+x$
F	$0.003913-x$		$0.00633-x$		x

Table S1. Gypsum precipitation according to the ICE (Initial, Change, Equilibrium) framework, except that "Equilibrium" (E) is replaced with "Final" (F) since the system does not reach equilibrium while within the module. The estimated Gypsum precipitation from a solution of Ca^{2+} & SO_4^{2-} – based upon the K_{sp} of Gypsum and the activity coefficients of this solution from iPHREEQC – is derived in S6 for the system in this table.

Alternative permeate flux distribution One method assumes that permeate flux decreases linearly along the RO module. This causes the concentration to increase exponentially along the RO module. The concentration is quantitatively tracked as the concentration factor (CF), which describes the concentration a feed corpuscle relative to the influent concentration

$$CF = \frac{initial}{final} \tag{S1}$$

as the quotient of initial to final ionic concentrations (influent vs. effluent) (2), solution masses, or permeate moles. The negative slope of permeate flux is calculated between the first cell 1 and the last cell n

$$slope = \frac{(\Delta\Phi_n - \Delta\Phi_1)}{n}\ . \tag{S2}$$

The permeate fluxes in these border cells, $\Delta\Phi_1$ and $\Delta\Phi_n$, are calculated through a system of equations. One of these equations

$$\Delta\Phi_e = \frac{\Delta\Phi_{module}}{n} = \frac{\Delta\Phi_n + \Delta\Phi_1}{2} \tag{S3}$$

equates two definitions of the average permeate flux per cell e: 1) $\Delta\Phi_e = \frac{\Delta\Phi_{module}}{n}$ from the total permeate flux over the module $\Delta\Phi_{module}$, and 2) $\frac{\Delta\Phi_n+\Delta\Phi_1}{2}$, as the average between the border cells. The other equation is the definition of relative pressure loss over the RO module (3; 4) ($HL; 0 \leq HL \leq 1$) per **??**,

$$\Delta\Phi_n = \Delta\Phi_1 * (1 - HL), \tag{S4}$$

which is $\approx 10\%$ for most RO modules (5). The substitution of eq. (S4) into eq. (S3) – given HL, $\Delta\Phi_{module}$, and n – permits calculating $\Delta\Phi_1$ and $\Delta\Phi_n$, the flux slope of eq. (S2), and subsequently $\Delta\Phi_e$ from a linear expression of permeate flux per module cell

$$\Delta\Phi_e = (slope * e + \Delta\Phi_1). \tag{S5}$$

The calculation sequence for this permeate flux method is summarized:

1. Define HL, $\Delta\Phi_{module}$, and n
2. Calculate the permeate flux slope [eqs. (S2) to (S4)]
3. Calculate the permeate flux in each cell e [eq. (S5)]

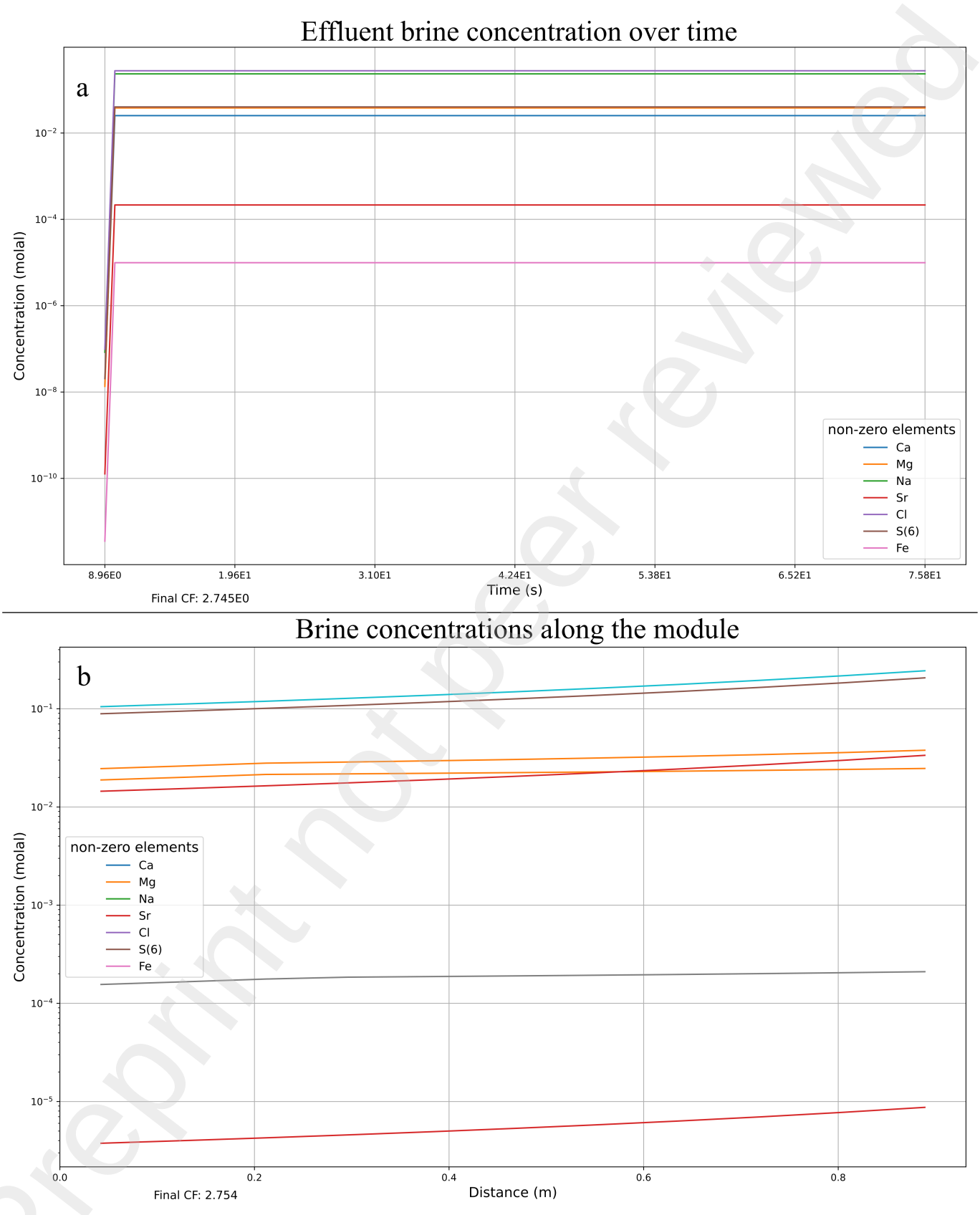

Figure S1. Brine formation while slicing through either a) time at the final cell or b) distance at the final time. The end concentrations slightly differ between these two simulation perspectives, where the all_time perspective calculates the true end of the last cell while the all_distance perspective calculates the mid-point of the last cell and thus has a slightly lower concentration. The brine represents desalination of the Red Sea through the BW30-400 module.

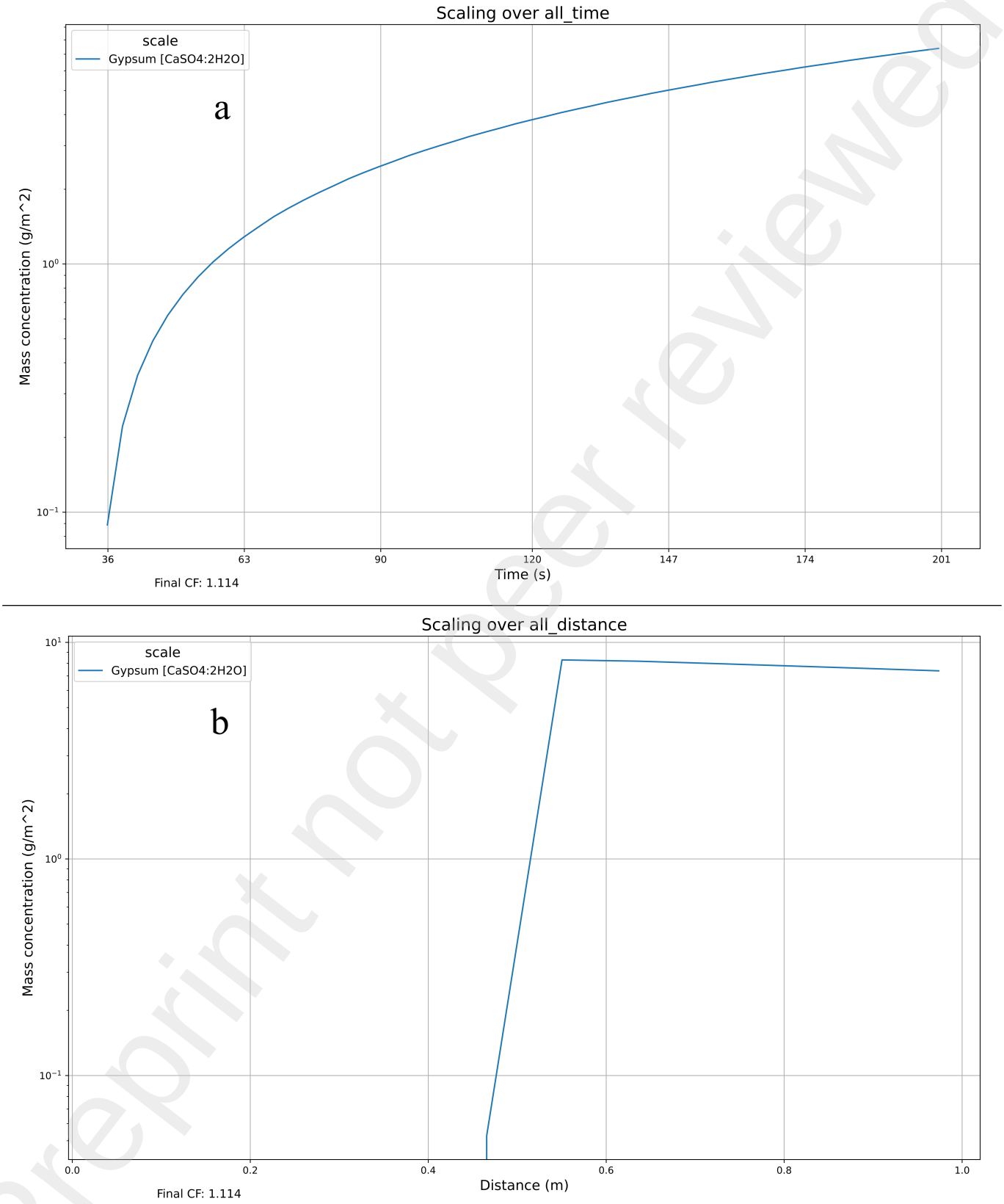

Figure S2. Scaling while either slicing through a) time at the final cell or b) distance at the final time. The underlying simulation was of the Red Sea through the BW30-400 module.

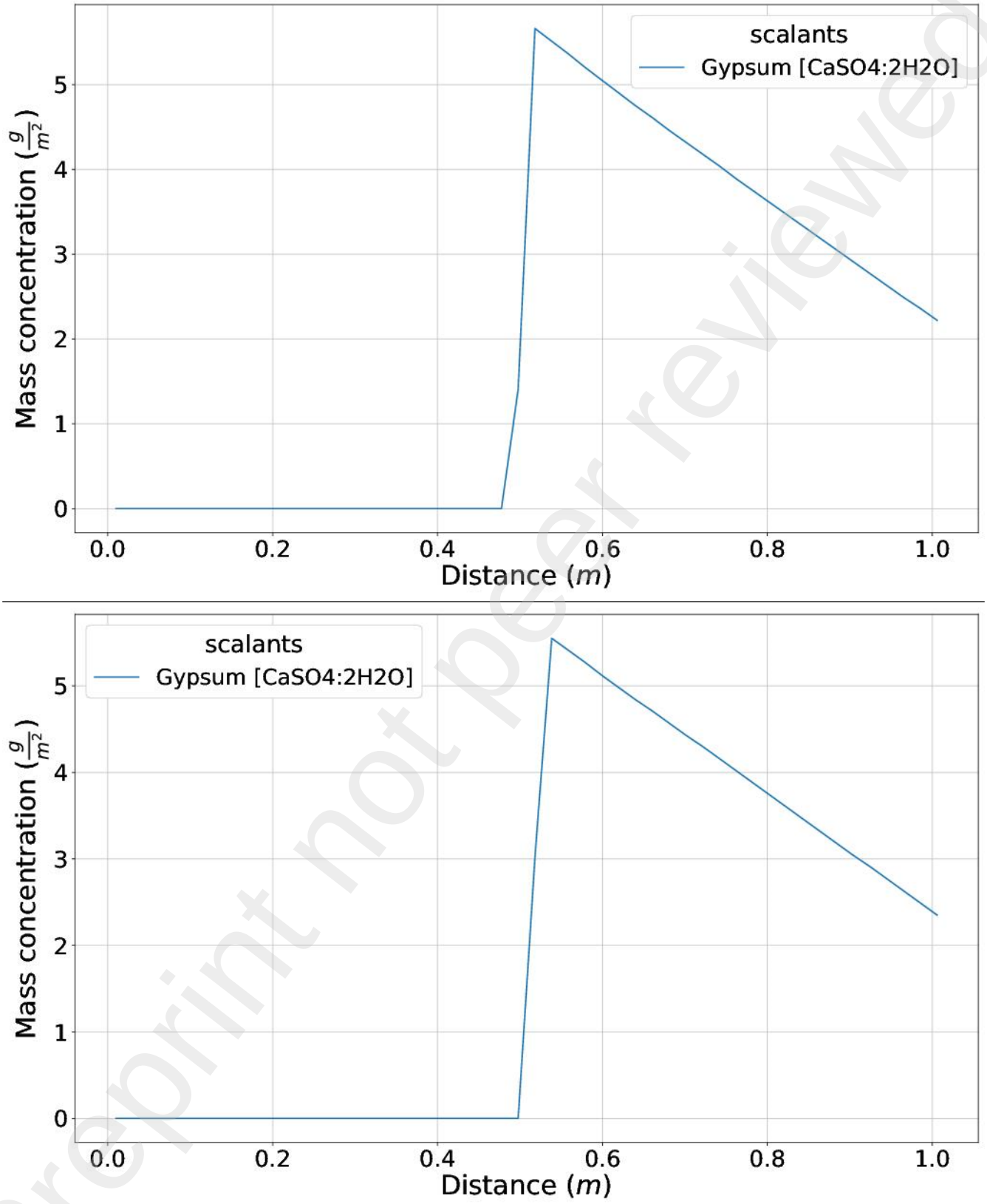

Figure S3. Predicted scaling of the Red Sea at $CF_{effluent} = 1.114$ via the linear CF (top) and linear permeate (bottom) flux methods. The exponential increase in CF that results from the linear permeate method skews scaling to the module end, relative to the linear CF method. This subtle difference in scaling distribution, nevertheless, neutralizes over the entire module and both methods quantitatively predict the same quantity of scale, which is elaborated in **??**.

	Ca^{2+}	+	SO_4^{2-}	$\leftrightharpoons$	$CaSO_4$
I	0.3545		1.816		0
C	−0.01859		−0.01859		+0.01961
F	0.3360		1.797		0.01961

Table S2. Gypsum precipitation according to the ICE (Initial, Change, Equilibrium) framework, except that "Equilibrium" (E) is replaced with "Final" (F) since the system does not completely reach equilibrium within the RO module. The 5%-error in row C, between the changes in ionic and Gypsum moles, suggests a subtle discrepancy in mass balance of PHREEQC; however, this is attributed to PHREEQC printing values before diffusion is incorporated in the calculations, per David Parkhurst.

2.1 ICE table calculations

The expected precipitation in the ICE table of Table S1 was determined as x in the following derivation:

$$\begin{aligned}
K_{sp} &= [a_{Ca^{2+}} - x]^1 * [a_{SO_4^{2-}} - x]^1 \\
K_{sp} &= (\gamma * [Ca^{2+}] - x) * (\gamma * [SO_4^{2-}] - x) \\
10^{-4.58} &= ((0.19 * 0.020594) - x) * ((0.06 * 0.105462) - x) \\
10^{-4.58} &= (0.003913 - x) * (0.00633 - x) \\
10^{-4.58} &= 2.477E-5 - 0.01024 + X^2 \\
0 &= -1.54E-6 - 0.01022x + x^2 \\
\therefore\ x &= 0.0104\ molal = \frac{\boxed{0.181\ \text{moles}}}{17.67\ kg\ water}\ .
\end{aligned} \tag{S6}$$

The activity coefficients (γ) for Ca^{2+} and SO_4^{2-} were sourced from PHREEQC for this specific solution system. The 17.67 kg mass of water corresponds to the mass maximum capacity of the simulated BW30-400 module.

The predicted precipitation in the presented ICE table of Table 1b ($gypsum\_pore\_volume$) are similarly derived:

$$\begin{aligned}
gypsum_pore_volume &= gypsum_all_shifts * \frac{cells_per_module}{total_simulation_shifts} \\
&= \sum_{i=1}^{n} (Gypsum_i) * \frac{12}{51} \\
&= 0.823 * \frac{12}{51} \\
&= 0.194\ moles\ .
\end{aligned} \tag{S7}$$

The $\frac{12}{51}$ fraction normalizes the quantity of scaling to that from a single pore volume through the module, instead of assessing the complete accumulation of scale from all pore volumes.

2.2 Evaporation versus transport desalination

The mechanism of concentrating a solution, either via evaporation or desalination, should not alter scaling predictions, ceterius paribus. Figure S4 contrasts scaling predictions from evaporation and desalination of the Red Sea, where the two mechanisms are approximately equivalent. Differences are postulated to originate from transport advection that is absent in evaporation.

3 In-series RO arrangements

In-series arrangements of multiple RO modules are represented by compounding individual modules. We determined that this approach is preferential to amplifying the characteristics of a single RO module – such as those in Table S3 of the DOW FILMTEC BW30-400 RO module similar to other models (1) – by a scalar $r = \frac{\Phi_{\Delta multi-module}}{\Phi_{\Delta module}}$, where $\Delta\Phi_{multi-module}$ is the total permeate flux of the multi-module system. The substitution of CF_{multi} for CF_e and $\Delta\Phi_{multi-module}$ for Φ_e into eq. (9) permits calculating the $\Delta\Phi_{multi-module}$.

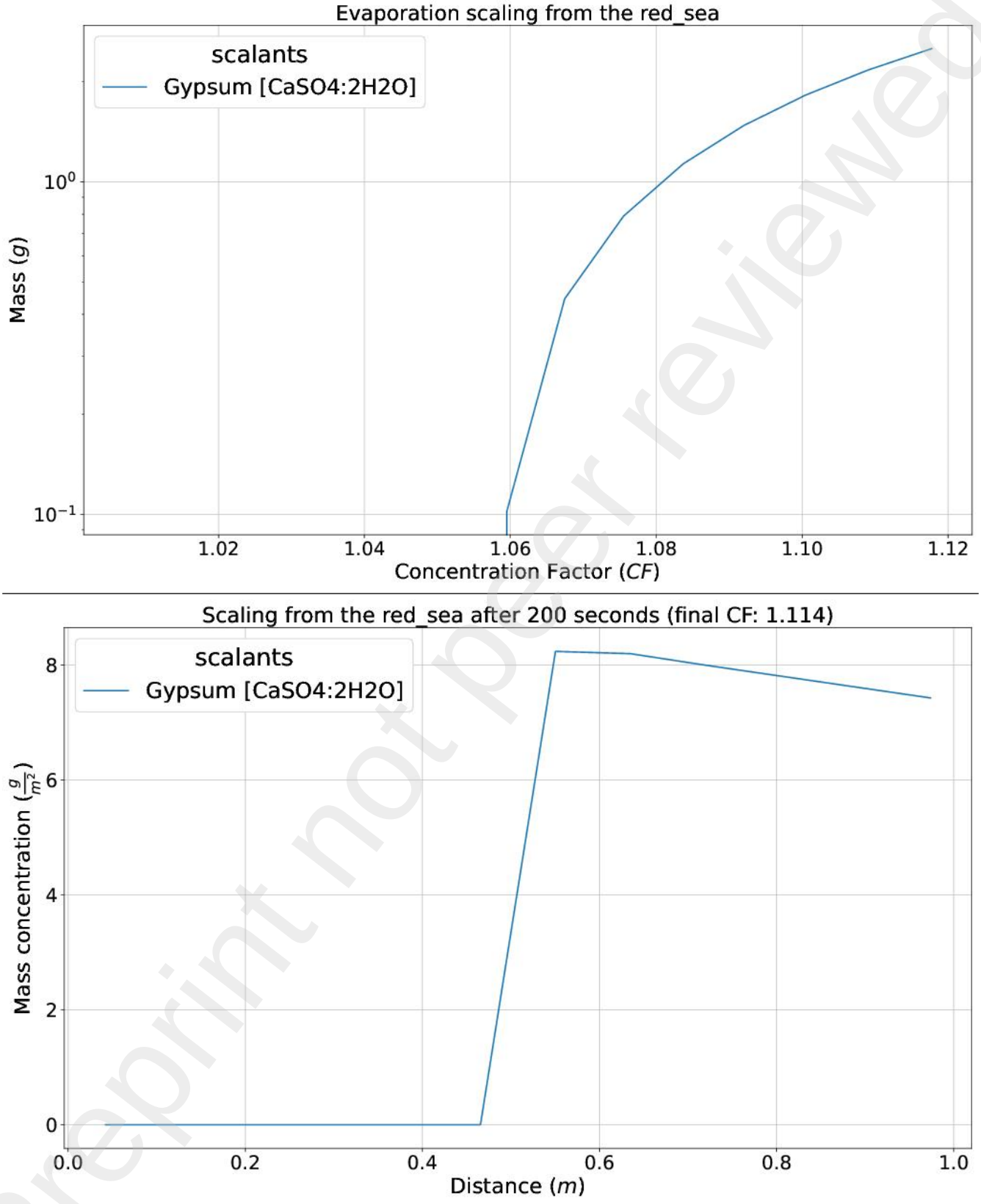

Figure S4. Scaling while a) evaporating and b) desalinating the Red Sea. The two scaling predictions are qualitatively similar, however, even after accounting for the accumulation amongst different pore volumes, the evaporation predictions ($3.36g$) are less than those of the reaction transport simulation ($5.27g$). The difference may be the absence of advection in the evaporation analysis.

Parameter	Value	Source
Module (m)		
length	1.016	BW30-400 (6)
diameter	0.201	BW30-400 (6)
permeate tube diameter	0.029	BW30-400 (6)
Membrane (mm)		
filtration layer	0.00025	(7; 8)
Feed spacer	0.8636	BW30-400 (6) & (9)
Permeate spacer	0.3	
Polysulphonic layer	0.05	
Support layer	0.15	
Windings $\left(\frac{th_{total}}{th_{membrane}}\right)$	86	BW30-400 (6)
Membrane cross-section (m^2)		
Module	0.0317	BW30-400 (6)
Permeate tube	0.000661	BW30-400 (6)
Filtration section	0.0311	BW30-400 (6)
Feed channel	0.0157	BW30-400 (6)
Feed channel capacity		
Volume (m^3)	0.0159	BW30-400 (6)
Mass (kg)	15.86	BW30-400 (6)
Fluid flow ($\frac{m^3}{second}$)		
Permeate	0.000463	BW30-400 (6)
Max Feed	0.00442	BW30-400 (6)

Table S3. Default dimensions of an RO module, with corresponding citations, that are primarily based upon the DOW FILMTEC BW30-400 RO module, following precedence from other software (1).

4 Water bodies

Feed parameters for an arbitrary water source can be composed by emulating the structure of the default feed parameter files that are provided with ROSSpy. Literature sources in Table S4 may be curated to construct feed parameter files for the respective feed sources.

Water body	Geochemical measurements
Indian Ocean	(10; 11; 12; 13; 14; 15; 16; 17)
Sargasso Sea	(18; 19)
South China Sea	(20; 21; 22; 23; 24)
Greek Coast	(25; 26; 27)
Toyko Bay	(28)
California Coast	(29; 30; 31)
North Atlantic	(32; 33; 34; 35; 36; 37; 38; 39; 40)
Baltic Sea	(41; 42)
North Pacific	(43; 44)
South Pacific	(45; 46)
General natural waters	(47; 48; 49; 50; 51; 52; 53)
Mississippi Salt Dome Basin	(54)

Table S4. Proposed literature of potential feed water that can be adapted into parameter files for simulation in our model, or specifically ROSSpy.

References

1. Li, M. Optimal plant operation of brackish water reverse osmosis (BWRO) desalination. *Desalination* **293**, 61–68, DOI: 10.1016/j.desal.2012.02.024 (2012).

2. Casas, S., Aladjem, C., Cortina, J. L., Larrotcha, E. & Cremades, L. V. Seawater Reverse Osmosis Brines as a New Salt Source for the Chlor-Alkali Industry: Integration of NaCl Concentration by Electrodialysis. *Solvent Extraction Ion Exchange* **30**, 322–332, DOI: 10.1080/07366299.2012.686849 (2012).

3. Srivathsan, G., Sparrow, E. M. & Gorman, J. M. Reverse osmosis issues relating to pressure drop, mass transfer, turbulence, and unsteadiness. *Desalination* **341**, 83–86, DOI: 10.1016/j.desal.2014.02.021 (2014).

4. Gu, J., Luo, J., Li, M., Huang, C. & Heng, Y. Modeling of pressure drop in reverse osmosis feed channels using multilayer artificial neural networks. *Chemical Engineering Research Design* **159**, 146–156, DOI: 10.1016/j.cherd.2020.04.019 (2020).

5. Fraidenraich, N., Vilela, O. C., Lima, G. A. & Gordon, J. M. Reverse osmosis desalination: Modeling and experiment. *Applied Physics Letters* **94**, 124102, DOI: 10.1063/1.3109795 (2009).

6. FilmTec ™ Membranes: FilmTec ™ BW30-400 high resolution, high surface area brackish water RO element. Tech. Rep., Du Pont (2020).

7. Pacheco, F. A., Pinnau, I., Reinhard, M. & Leckie, J. O. Characterization of isolated polyamide thin films of RO and NF membranes using novel TEM techniques. *Journal Membrane Science* **358**, 51–59, DOI: 10.1016/j.memsci.2010.04.032 (2010).

8. Jeong, B. H. *et al.* Interfacial polymerization of thin film nanocomposites: A new concept for reverse osmosis membranes. *Journal Membrane Science* **294**, 1–7, DOI: 10.1016/j.memsci.2007.02.025 (2007).

9. Sablani, S. S., Goosen, M. F., Al-Belushi, R. & Gerardos, V. Influence of spacer thickness on permeate flux in spiral-wound seawater reverse osmosis systems. *Desalination* **146**, 225–230, DOI: 10.1016/S0011-9164(02)00477-0 (2002).

10. Danielsson, L. G. Cadmium, cobalt, copper, iron, lead, nickel and zinc in Indian Ocean water. *Marine Chemistry* **8**, 199–215, DOI: 10.1016/0304-4203(80)90010-9 (1980).

11. Nisha, V. & Achyuthan, H. Geochemical evaluation of sea surface sediments along the continental shelf, south east coast of India. *Indian Journal Geo-Marine Sciences* **43**, 241–251 (2014).

12. Stephen-Pichaimani, V., Jonathan, M. P., Srinivasalu, S., Rajeshwara-Rao, N. & Mohan, S. P. Enrichment of trace metals in surface sediments from the northern part of Point Calimere, SE coast of India. *Environmental Geology* **55**, 1811–1819, DOI: 10.1007/s00254-007-1132-9 (2008).

13. Selvaraj, K., Ram Mohan, V. & Szefer, P. Evaluation of metal contamination in coastal sediments of the Bay of Bengal, India: Geochemical and statistical approaches. *Marine Pollution Bulletin* **49**, 174–185, DOI: 10.1016/j.marpolbul.2004.02.006 (2004).

14. Thangadurai, N., Srinivasalu, S., Jonathan, M. P., Rajeshwara Rao, N. & Santhosh Kumar, R. Pre-tsunami chemistry of sediments along the inner continental shelf off Ennore, Chennai, southeast coast of India. *Indian Journal Marine Sciences* **34**, 274–278 (2005).

15. Parvez Al-Usmani, S. M., Jagtap, T. G. & Patil, D. N. Trace metals in water, sediment and bivalves of a tropical estuary, west coast of India. *Marine Pollution Bulletin* **99**, 328–331, DOI: 10.1016/j.marpolbul.2015.07.036 (2015).

16. Sabine, C. L., Key, R. M., Feely, R. A. & Greeley, D. Inorganic carbon in the Indian Ocean: Distribution and dissolution processes. *Global Biogeochemical Cycles* **16**, 15–1, DOI: 10.1029/2002gb001869 (2002).

17. Singh, S. P., Singh, S. K. & Bhushan, R. Internal cycling of dissolved barium in water column of the Bay of Bengal. *Marine Chemistry* **154**, 12–23, DOI: 10.1016/j.marchem.2013.04.013 (2013).

18. Bender, M. L. & Gagner, C. Dissolved copper, nickel, and cadmium in the Sargasso Sea. *Journal Marine Research* **34**, 327–339 (1976).

19. Stoffyn-Egli, P. & Mackenzie, F. T. Mass balance of dissolved lithium in the oceans. *Geochimica et Cosmochimica Acta* **48**, 859–872, DOI: 10.1016/0016-7037(84)90107-8 (1984).

20. Calvert, S. E., Pedersen, T. F. & Thunell, R. C. Geochemistry of the surface sediments of the Sulu and South China Seas. *Marine Geology* **114**, 207–231, DOI: 10.1016/0025-3227(93)90029-U (1993).

21. Wen, L. S., Jiann, K. T. & Santschi, P. H. Physicochemical speciation of bioactive trace metals (Cd, Cu, Fe, Ni) in the oligotrophic South China Sea. *Marine Chemistry* **101**, 104–129, DOI: 10.1016/j.marchem.2006.01.005 (2006).

22. Du, C. *et al.* Dynamics of dissolved inorganic carbon in the South China Sea: A modeling study. *Progress Oceanography* **186**, 102367, DOI: 10.1016/j.pocean.2020.102367 (2020).

23. Chen, C. T. A., Wang, S. L., Wang, B. J. & Pai, S. C. Nutrient budgets for the South China sea basin. *Marine Chemistry* **75**, 281–300, DOI: 10.1016/S0304-4203(01)00041-X (2001).

24. Nakaguchi, Y., Takei, M., Hattori, H., Arii, Y. & Yamaguchi, Y. Dissolved selenium species in the Sulu Sea, the South China Sea and the Celebes Sea. *Geochemical Journal* **38**, 571–580, DOI: 10.2343/geochemj.38.571 (2004).

25. Chester, R. & Voutsinou, F. G. The initial assessment of trace metal pollution in coastal sediments. *Marine Pollution Bulletin* **12**, 84–91, DOI: 10.1016/0025-326X(81)90198-3 (1981).

26. Voutsinou-Taliadouri, F. & Satsmadjis, J. Distribution of heavy metals in sediments of the Patraikos gulf (Greece). *Marine Pollution Bulletin* **14**, 33–35, DOI: 10.1016/0025-326X(83)90094-2 (1983).

27. Voutsinou-Taliadouri, F., Varnavas, S. P., Nakopoulou, C. & Moriki, A. Dissolved trace elements in south Aegean seawater. *Marine Pollution Bulletin* **34**, 840–843, DOI: 10.1016/S0025-326X(97)00070-2 (1997).

28. Fukushima, K., Saino, T. & Kodama, Y. Trace metal contamination in Tokyo Bay, Japan. *Science Total Environment, The* **125**, 373–389, DOI: 10.1016/0048-9697(92)90402-E (1992).

29. Hershelman, G. P., Schafer, H. A., Jan, T. K. & Young, D. R. Metals in marine sediments near a large California municipal outfall. *Marine Pollution Bulletin* **12**, 131–134, DOI: 10.1016/0025-326X(81)90442-2 (1981).

30. Luoma, S. N. & Phillips, D. J. Distribution, variability, and impacts of trace elements in San Francisco Bay. *Marine Pollution Bulletin* **19**, 413–425, DOI: 10.1016/0025-326X(88)90396-7 (1988).

31. Biller, D. V. & Bruland, K. W. Sources and distributions of Mn, Fe, Co, Ni, Cu, Zn, and Cd relative to macronutrients along the central California coast during the spring and summer upwelling season. *Marine Chemistry* **155**, 50–70, DOI: 10.1016/j.marchem.2013.06.003 (2013).

32. Loring, D. H. Geochemistry of Zinc, Copper and Lead in the Sediments of the Estuary and Gulf of St. Lawrence. *Can J Earth Sci* **15**, 757–772, DOI: 10.1139/e78-082 (1978).

33. Loring, D. H. Geochemistry of cobalt, nickel, chromium, and vanadium in the sediments of the estuary and open gulf of St. Lawrence. *Can J. Earth Sci.1* **16**, 1196–1209 (1979).

34. Yeats, P. A. & Bewers, J. M. Potential Anthropogenic Influences on Trace Metal Distributions in the North Atlantic. *Canadian Journal Fisheries Aquatic Sciences* **40**, 124–131, DOI: 10.1139/f83-318 (1983).

35. Bothner, M. H., Buchholtz Ten Brink, M. & Manheim, F. T. Metal concentrations in surface sediments of Boston Harbor - Changes with time. *Marine Environmental Research* **45**, 127–155, DOI: 10.1016/S0141-1136(97)00027-5 (1998).

36. Campbell, J. A. & Loring, D. H. Baseline levels of heavy metals in the waters and sediments of Baffin Bay. *Marine Pollution Bulletin* **11**, 257–261, DOI: 10.1016/0025-326X(80)90314-8 (1980).

37. Gaulier, C. *et al.* Trace metal speciation in North Sea coastal waters. *Science Total Environment* **692**, 701–712, DOI: 10.1016/j.scitotenv.2019.07.314 (2019).

38. Statham, P. J. & Burton, J. D. Dissolved manganese in the North Atlantic Ocean, 0-35°N. *Earth Planetary Science Letters* **79**, 55–65, DOI: 10.1016/0012-821X(86)90040-3 (1986).

39. Mohamed, K. N., Steigenberger, S., Nielsdottir, M. C., Gledhill, M. & Achterberg, E. P. Dissolved iron(III) speciation in the high latitude North Atlantic Ocean. *Deep-Sea Research Part I: Oceanographic Research Papers* **58**, 1049–1059, DOI: 10.1016/j.dsr.2011.08.011 (2011).

40. Guay, C. K. & Falkner, K. K. A survey of dissolved barium in the estuaries of major Arctic rivers and adjacent seas. *Continental Shelf Research* **18**, 859–882, DOI: 10.1016/S0278-4343(98)00023-5 (1998).

41. Szefer, P., Kusak, A., Szefer, K., Jankowska, H. & WoŁowicz, M. Distribution of selected metals in sediment cores of puck bay, Baltic Sea. *Marine Pollution Bulletin* **30**, 615–618, DOI: 10.1016/0025-326X(95)00079-3 (1995).

42. Kremling, K. & Petersen, H. The distribution of Mn, Fe, Zn, Cd and Cu in Baltic seawater; a study on the basis of one anchor station. *Marine Chemistry* **6**, 155–170, DOI: 10.1016/0304-4203(78)90025-7 (1978).

43. Tanita, I., Takeda, S., Sato, M. & Furuya, K. Surface and middle layer enrichment of dissolved copper in the western subarctic North Pacific. *Mer* **53**, 1–18 (2015).

44. Sim, N. & Orians, K. J. Annual variability of dissolved manganese in Northeast Pacific along Line-P: 2010–2013. *Marine Chemistry* **216**, 103702, DOI: 10.1016/j.marchem.2019.103702 (2019).

45. Boyle, E. & Edmond, J. M. Copper in surface waters south of New Zealand. *Nature* **253**, 107–109, DOI: 10.19004/pjssz.51.0{_}75{_}3 (1975).

46. Boyle, E. A., Sclater, F. & Edmond, J. M. On the marine geochemistry of cadmium. *Nature* **263**, 42–44, DOI: 10.19592/j.cnki.scje.2017.03.002 (1976).

47. Alibo, D. S. & Nozaki, Y. Rare earth elements in seawater: Particle association, shale-normalization, and Ce oxidation. *Geochimica et Cosmochimica Acta* **63**, 363–372, DOI: 10.1016/S0016-7037(98)00279-8 (1999).

48. Klinkhammer, G., Elderfield, H. & Hudson, A. Rare earth elements in seawater near hydrothermal vents. *Nature* **305**, 185–188, DOI: 10.1038/305185a0 (1983).

49. Garcia-Solsona, E. *et al.* Rare earth elements and Nd isotopes as tracers of modern ocean circulation in the central Mediterranean Sea. *Progress Oceanography* **185**, 102340, DOI: 10.1016/j.pocean.2020.102340 (2020).

50. Longinelli, A. & Craig, H. Oxygen-18 Variations in sulfate ions in sea water and saline lakes. *Science* **156**, 56–59 (1967).

51. Llyod, R. M. Oxygen-18 Composition of Oceanic Sulfate. *Science* **156**, 1228–1231, DOI: 10.1126/science.156.3779.1228 (1967).

52. Culkin, F. & Cox, R. A. Sodium, potassium, magnesium, calcium and strontium in sea water. *Deep-Sea Research Oceanographic Abstracts* **13**, 789–804, DOI: 10.1016/0011-7471(76)90905-0 (1966).

53. Krumgalz, B. S. Calcium distribution in the world ocean waters. *Oceanologica Acta* **5**, 121–128 (1982).

54. Kharaka, Y. K. *et al.* Geochemistry of metal-rich brines from central Mississippi Salt Dome basin, U.S.A. *Applied Geochemistry* **2**, 543–561, DOI: 10.1016/0883-2927(87)90008-4 (1987).